

# Computed Tomography

---

R.M. Leahy

*University of Southern  
California*

R. Clackdoyle

*CNRS, France*

1	Introduction.....	1155
2	Background.....	1155
	2.1 X-ray Computed Tomography • 2.2 Nuclear Imaging Using PET and SPECT • 2.3 Mathematic Preliminaries • 2.4 Examples	
3	2D Image Reconstruction.....	1159
	3.1 Fourier Space and Filtered Backprojection Methods for Parallel-Beam Projections • 3.2 Fan-Beam Filtered Backprojection	
4	Extending 2D Methods into 3D.....	1163
	4.1 Extracting 2D Data from 3D • 4.2 Spiral CT • 4.3 Rebinning Methods in 3D PET	
5	3D Image Reconstruction.....	1165
	5.1 Fully 3D Reconstruction with Missing Data • 5.2 Cone-Beam Tomography	
6	Iterative Reconstruction Methods.....	1168
	6.1 Finite Dimensional Formulations and ART • 6.2 Statistical Formulations • 6.3 Maximum Likelihood Methods • 6.4 Bayesian Reconstruction Methods	
7	Summary.....	1171
	References.....	1172

## 1 Introduction

---

The term *tomography* refers to the general class of devices and procedures for producing two-dimensional (2D) cross-sectional images of a three-dimensional (3D) object. Tomographic systems make it possible to image the internal structure of objects in a non-invasive and non-destructive manner. By far the best known application is the computer assisted tomography (CAT or simply CT) scanner for x-ray imaging of the human body. Other medical imaging devices, including PET (positron emission tomography), SPECT (single photon emission computed tomography) and MRI (magnetic resonance imaging) systems, also make use of tomographic principles. Outside of the biomedical realm, tomography is used in diverse applications such as microscopy, non-destructive testing, radar imaging, geophysical imaging and radio astronomy.

We will restrict our attention here to image reconstruction methods for x-ray CT, PET and SPECT. In all three modalities the data can be modeled as a collection of line integrals of the unknown image. Many of the methods described here can also be applied to other tomographic problems. However, the reader should refer to Chapter 3.6 for a more general

treatment of image reconstruction in the context of ill-posed inverse problems.

We describe 2D image reconstruction from parallel and fan-beam projections and 3D reconstruction from sets of 2D projections. Algorithms derived from the analytic relationships between functions and their line integrals, the so called “direct methods”, are described in Sections 3–5. In Section 6 we describe the class of “iterative methods” that are based on a finite dimensional discretization of the problem. We will include key results and algorithms for a range of imaging geometries, including systems currently in development. References to the appropriate sources for a complete development are also included. Our objective is to convey the wide range of methods available for reconstruction from projections and to highlight some recent developments in what remains a highly active area of research.

## 2 Background

---

### 2.1 X-ray Computed Tomography

In conventional x-ray radiography, a stationary source and planar detector are used to produce a 2D projection image of

the patient. The image has intensity proportional to the amount by which the x-rays are attenuated as they pass through the body, i.e., the 3D spatial distribution of x-ray attenuation coefficients is projected into a 2D image. The resulting image provides important diagnostic information due to differences in the attenuation coefficients of bone, muscle, fat and other tissues in the 40–120 keV range used in clinical radiography [1].

X-rays passing through an object experience exponential attenuation proportional to the linear attenuation coefficient of the object. The intensity of a collimated beam of monoenergetic x-radiation exiting a uniform block of material with linear attenuation coefficient  $\mu$  and depth  $d$  is given by  $I = I_0 e^{-\mu d}$  where  $I_0$  is the intensity of the incident beam. For objects with spatially variant attenuation  $\mu(z)$  along the path length  $z$ , this relationship generalizes to:

$$I = I_0 e^{-\int \mu(z) dz} \quad (1)$$

where  $\int \mu(z) dz$  is a *line integral* through  $\mu(z)$ .

Let  $\mu(x, y, z)$  represent the 3D distribution of attenuation coefficients within the human body. Consider a simplified model of a radiography system that produces a broad parallel-beam of x-rays passing through the patient in the  $z$  direction. An ideal 2D detector array or film in the  $(x, y)$ -plane would produce an image with intensity proportional to the negative logarithm of the attenuated x-ray beam, i.e.,  $-\log(I/I_0)$ . The following projection image would then be formed at the ideal detector:

$$r(x, y) = \int \mu(x, y, z) dz \quad (2)$$

The utility of conventional radiography is limited due to the projection of 3D anatomy into a 2D image, causing certain

structures to be obscured. For example, lung tumors, which have a higher density than the surrounding normal tissue, may be obscured by a more dense rib that projects into the same area in the radiograph. Computed tomography (CT) systems overcome this problem by reconstructing 2D cross-sections of the 3D attenuation coefficient distribution.

The concept of the line integral is common to both the radiographic projection (2) and computed tomography. Consider the first clinical x-ray CT system for which the inventor, G. Hounsfield, received the 1979 Nobel Prize in medicine (the prize was shared with the mathematician A. Cormack) [2]. A collimated x-ray source and detector are translated on either side of the patient so that a single plane is illuminated, as illustrated in Fig. 1a. After applying a logarithmic transformation, the detected x-ray measurements are a set of line integrals representing a 1D parallel projection of the 2D x-ray attenuation coefficient distribution in the illuminated plane. By rotating the source and detector around the patient other 1D projections can be measured in the same plane. The image can then be reconstructed from these *parallel-beam* projections using the methods described in Section 3.1.

One major limitation of the first generation of CT systems was that the translation and rotation of the detectors was slow and a single scan would take several minutes. X-ray projection data can be collected far more quickly using the *fan-beam* x-ray source geometry employed in the current generation of CT scanners as illustrated in Fig. 1b. Since an array of detectors is used, the system can simultaneously collect data for all projection paths that pass through the current location of the x-ray source. In this case, the x-ray source need not be translated and a complete set of data is obtained through a single rotation of the source around the patient. Using this configuration modern scanners can scan a

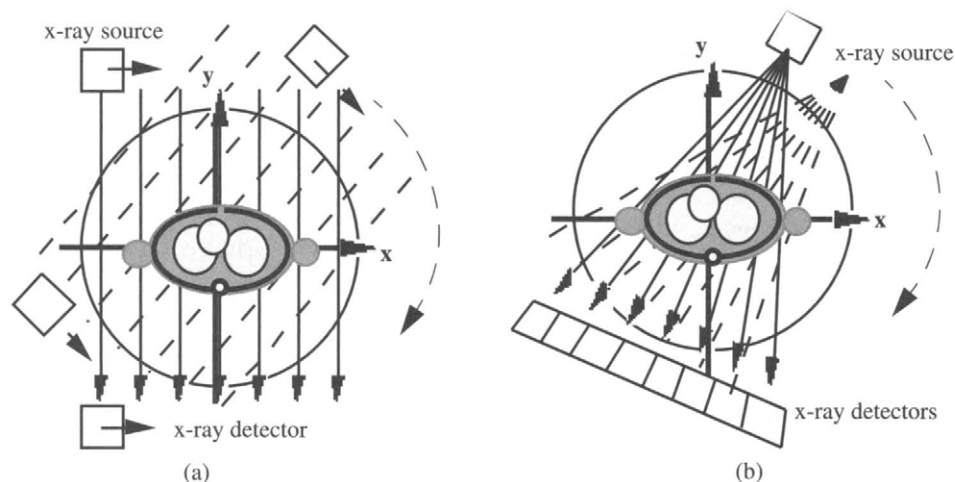


**FIGURE 1** (a) Schematic representation of a first generation CT scanner that uses translation and rotation of the source and a single detector to collect a complete set of 1D parallel projections; (b) the current generation of CT scanners use a fan x-ray beam and an array of detectors, which requires rotation only.

single plane in less than one second. Methods for reconstruction from fanbeam data are described in Section 3.2.

Recently developed spiral CT systems allow continuous acquisition of data as the patient bed is moved through the scanner [3]. The detector traces out a helical orbit with respect to the patient allowing rapid collection of projections over a 3D volume. These data require special reconstruction algorithms as described in Section 4.2. In an effort to simultaneously collect fully 3D CT data, a number of systems have been developed that use a *cone-beam* of x-rays and a 2D rather than 1D array of detectors [3]. While cone-beam systems are rarely used in clinical CT, they do play an important role in industrial applications. Methods for cone-beam reconstruction are described in Section 5.2.

The above descriptions can only be considered approximate because a number of factors complicate the x-ray CT problem. For example, the x-ray beam typically contains a broad spectrum of energies and therefore an energy dependence should be included in (1) [1]. The theoretical development of CT methods usually assumes a monoenergetic source. For broadband x-ray sources, the beam becomes “hardened” as it passes through the object, i.e., the lower energies are attenuated faster than the higher energies. This effect causes a beam hardening artifact in CT images that is reduced in practice using a data calibration procedure [4].

In x-ray CT data the high photon flux produces relatively high signal to noise ratios. However, the data are corrupted by the detection of scattered x-rays that do not conform to the line integral model. Calibration procedures are required to compensate for this effect as well as for the effects of variable detector sensitivity. A final important factor in the acquisition of CT data is the issue of sampling. Each 1D projection is undersampled by approximately a factor of two in terms of the attainable resolution as determined by detector size. Methods to compensate for this problem in fan-beam systems using fractional detector offsets are described in [3].

## 2.2 Nuclear Imaging Using PET and SPECT

PET and SPECT are methods for producing images of the spatial distribution of biochemical tracers or probes that have been tagged with radioactive isotopes [1]. By tagging different molecules with positron or gamma-ray emitters, PET and SPECT can be used to reconstruct images of the spatial distribution of a wide range of biochemical probes. Applications include the use of tracers to measure glucose metabolism, angiogenesis and cell proliferation for the detection and staging of cancer, imaging of cardiac function, imaging of gene expression, and studies of neurochemistry using a range of neuro-receptors and transmitters [6–8]. In recent years, smaller animal versions of clinical scanners have been developed for research applications in drug development, studies of animal models of human disease, and genomic and proteomic studies in live animals [9].

SPECT systems detect emissions using a “gamma camera”. This camera is a combination of a sodium iodide scintillation crystal and an array of photomultiplier tubes (PMTs). The PMTs measure the location on the camera surface at which each gamma ray photon is absorbed by the scintillator [1]. A mechanical collimator, consisting of a sheet of dense metal in which a large number of parallel holes have been drilled, is attached to the front of the camera as illustrated in Fig. 2a. The collimated camera is only sensitive to gamma rays traveling in a direction parallel to the holes in the collimator. The total number of gamma rays detected at a given pixel in the camera will be approximately proportional to the total activity (or line integral) along the line that passes through the patient and is parallel to the holes in the collimator. Thus when viewing a patient from a fixed camera position, we collect a 2D projection image of the 3D distribution of the tracer. By collecting data as the camera is rotated to multiple positions around the patient, we obtain *parallel-beam* projections for a contiguous set of parallel 2D slices through

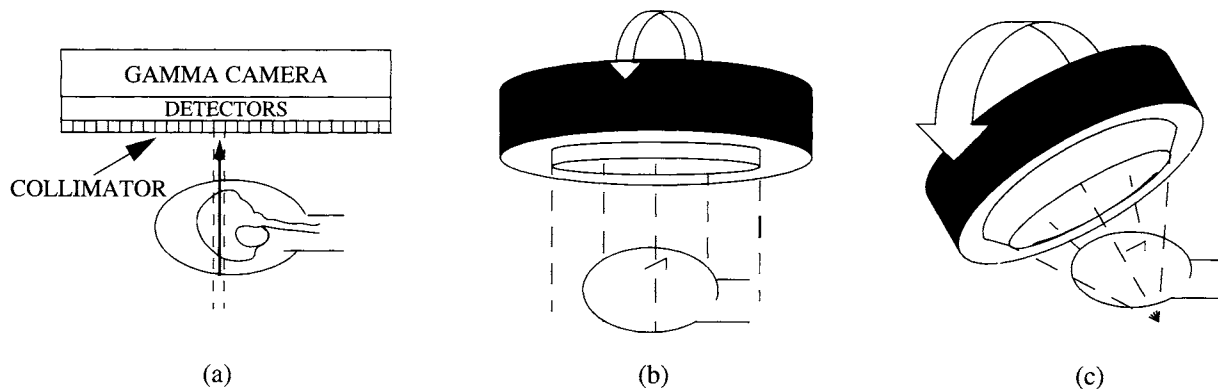


**FIGURE 2** Schematic representation of a SPECT system: (a) cross-sectional view of a system with parallel hole collimator: gamma rays normally incident to the camera surface are detected, others are stopped by the collimator so that the camera records parallel projections of the source distribution. (b) Rotation of the camera around the patient produces a complete set of parallel projections. (c) Different collimators can be used to collect converging or diverging fan and cone-beam projections; shown is a converging cone-beam collimator.

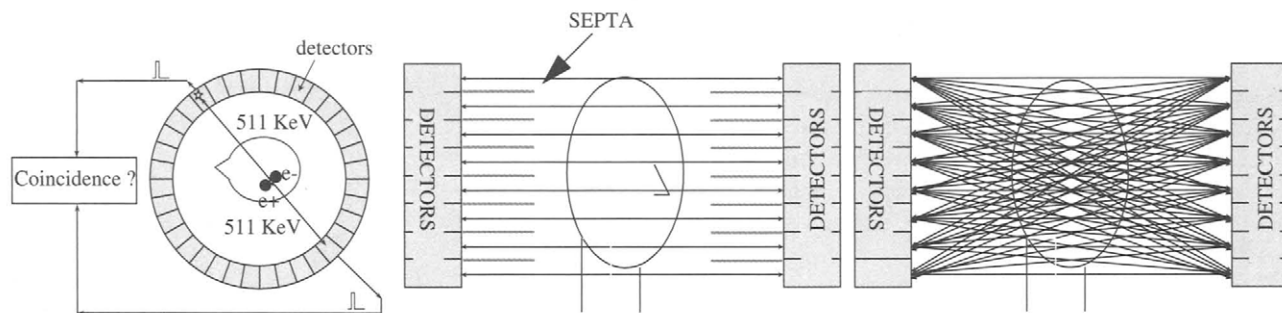


**FIGURE 3** (a) Schematic showing how coincidence detection of photon pair produced by electron-positron annihilation determines the line along which the positron was annihilated; (b) in 2D PET systems, septa between adjacent rings of detectors prevent coincidence detection between rings; (c) removal of the septa produces a fully 3D PET system in which cross-plane coincidences are collected and used to reconstruct the source distribution.

the patient, Fig. 2b. The distribution can be reconstructed slice-by-slice using the same parallel-beam reconstruction methods as are used for x-ray CT.

Other collection geometries can be realized by modifying the collimator design [6]. For imaging an organ, such as the brain or heart, that is smaller than the surface area of the camera, improved sensitivity can be realized by using converging *fan-beam* or *cone-beam* collimators as illustrated in Fig. 2c. Similarly, diverging collimators can be used for imaging larger objects. Images are reconstructed from these fan-beam and cone-beam data using the methods in Section 3.2 and Section 5.2, respectively. While the vast majority of SPECT systems use rotating planar gamma cameras, other systems have been constructed using a cylindrical scintillation detector that surrounds the patient. A rotating cylindrical collimator defines the projection geometry. Although the physical design of these cylindrical systems is quite different from that of the rotating camera, in most cases the reconstruction problem can still be reduced to one of the three basic forms: parallel, fan or cone-beam.

PET is based on the physical property that a positron produced by a radioactive nucleus travels a very short distance and then annihilates with an electron to form a pair of high energy (511 keV) photons [7]. The pair of photons travel in opposite directions along a straight line path. Detection of the positions at which the photon pair intersect a ring of detectors allows us to approximately define a line that contains the positron emitter, as illustrated in Fig. 3a. The total number of photon pairs measured by a detector pair will be proportional to the total number of positron emissions along the line joining the detectors, i.e., the number of detected events between a detector pair is an approximate line integral of the tracer density.

A PET scanner requires one or more rings of photon detectors coupled to a timing circuit that detects coincident photon pairs by checking that both photons arrive at the detectors within a few nanoseconds of each other. PET detectors are usually constructed using a combination of scintillation crystals and PMTs. A unique aspect of PET is that

the ring of detectors surrounding the subject allows simultaneous acquisition of a complete data set; no rotation of the detector system is required. A schematic view of two PET scanners is shown in Fig. 3. In the 2D scanner, multiple rings of detectors surround the patient with dense material, or “septa”, separating each ring. These septa stop photons traveling between rings so that coincidence events are collected only between pairs of detectors in a single ring. We refer to this configuration as a 2D scanner since the data are separable and the image can be reconstructed as a series of 2D sections. In contrast, the 3D scanners have no septa so that coincidence photons can be detected between planes. In this case the reconstruction problem is not separable and must be treated directly in 3D.

PET data can be viewed as sets of approximate line integrals. In 2D mode the data are sets of *parallel-beam* projections and the image can be reconstructed using methods equivalent to those in parallel-beam x-ray CT. In the 3D case, the data are still line integrals, but new algorithms are required to deal with the between-plane coincidences that represent *incomplete* projections through the patient. These methods are described in Sections 4 and 5.

As with x-ray CT, the line integral model is only approximate. Finite and spatially variant detector resolution is not accounted for in the line integral model and has a major impact on image quality [10]. The number of photons detected in PET and SPECT is relatively small so that photon limited noise is also a factor limiting image quality. The data are further corrupted by additional noise due to scattered photons. Also, in both PET and SPECT, the probability of detecting an emission is reduced by the relatively high probability of Compton scatter of photons before they reach the detector. These attenuation effects can be quantified by performing a separate “transmission” scan in which the scattering properties of the body are measured. This information must then be incorporated into the reconstruction algorithm [7, 10]. While all of these effects can, to some degree, be compensated for within the framework of analytic reconstruction from line integrals, they are more readily and

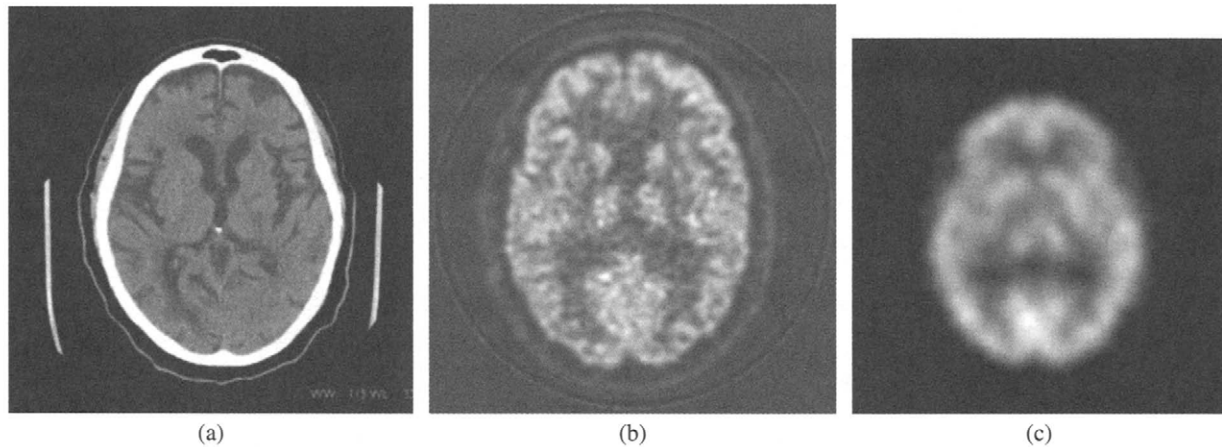


**FIGURE 4** Examples of brain scans using: (a) x-ray CT, a non-linear gray scale is used to enhance contrast between soft tissue regions within the brain; (b) PET, this image shows an image of glucose metabolism obtained using an analog of glucose labelled with the positron emitting isotope, flourine-18; (c) SPECT, this is a brain perfusion scan using a technitium-99m ligand (image courtesy of J. E. Bowsher, Duke University Medical Center).

accurately dealt with using the finite dimensional statistical formulations described in Section 6.

### 2.3 Mathematic Preliminaries

Since we deal with both 2D and 3D reconstruction problems here, we will use the following unified definition of the line integrals of an image  $f(x)$ :

$$g(a, \theta) = \int_{-\infty}^{\infty} f(a + t\theta) dt \quad \|\theta\| = 1 \quad (3)$$

Here  $g$  is the integral  $f$  of over the line passing through  $a$  and oriented in the direction  $\theta$ .

For parallel projections we consider only a fixed  $\theta$  (the projection direction). To avoid redundant parameterization of line integrals we only consider those  $a$  perpendicular to  $\theta$  (i.e.,  $a \cdot \theta = 0$ ). We say a parallel projection  $g(\cdot, \theta)$  is truncated if some non-zero line integrals are not measured. Generally, truncation is due to the use of a finite detector system which may be too small to gather a complete projection of the object at some orientation  $\theta$ .

For fan-beam and cone-beam systems, we consider  $a$  to be fixed for a single projection;  $a$  is the fan-vertex or cone-vertex, which in practice would be the position of the x-ray source or the focal point of a converging collimator. Again, truncation of a projection  $g(a, \cdot)$  refers to line integrals which are not available, typically due to the limited extent of the detector.

### 2.4 Examples

We conclude this introductory section with examples of CT, PET and SPECT images collected from the current generation of scanners. These images clearly reveal the differences

between the high resolution, low noise images produced by x-ray CT scanners, Fig. 4(a), and the lower resolution and noisy images produced by the nuclear imaging instruments, Figs. 4(b) and (c). These differences are primarily due to the photon flux in x-ray CT which is many orders of magnitude higher than the individually detected photons in nuclear medicine imaging. In diagnostic imaging these modalities are highly complementary since x-ray CT reveals information about the patients *anatomy* while PET and SPECT images contain *functional* information. For further insight into the ability of x-ray CT to produce high resolution anatomic images, we show a set of 3D renderings from CT data in Fig. 5.

## 3 2D Image Reconstruction

### 3.1 Fourier Space and Filtered Backprojection Methods for Parallel-Beam Projections

For 2D parallel-beam projections the general notation of (1) can be refined as illustrated in Fig. 6. We parameterize the direction of the rays using  $\phi$ , so  $\theta = (\cos \phi, \sin \phi)$ . For the position  $a$  perpendicular to  $\theta$ , we write  $a = (-u \sin \phi, u \cos \phi) = u\theta^\perp$  where  $u$  is the scalar coordinate indicating the distance from the origin to the integration line, or equivalently, the projection element index for the  $\phi$ -projection. Since  $\theta$  depends only on  $\phi$ , and  $a$  then depends on  $u$ , we simplify the notation by writing  $g(u, \phi) = g(a, \theta) = \int f(a + t\theta) dt$ . For the parallelbeam case the function  $g$  is the Radon transform of the image  $f$  [4].

Practical inversion methods can be developed using the relationship between the Radon and Fourier transforms. The projection slice theorem is the basic result that is used in developing these methods [4]. This theorem states that the 1D Fourier transform of the parallel projection at angle  $\phi$  is

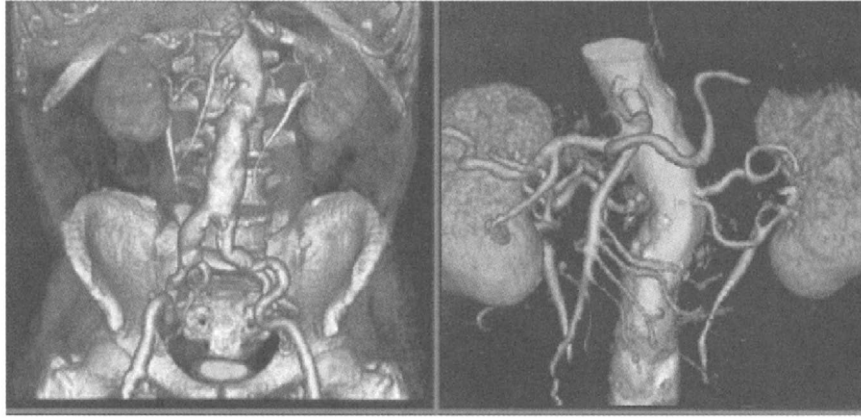


**FIGURE 5** Volume rendering from a sequence of x-ray CT images showing the abdominal cavity and kidneys (CT images courtesy of G. E. Medical Systems) (see color insert).

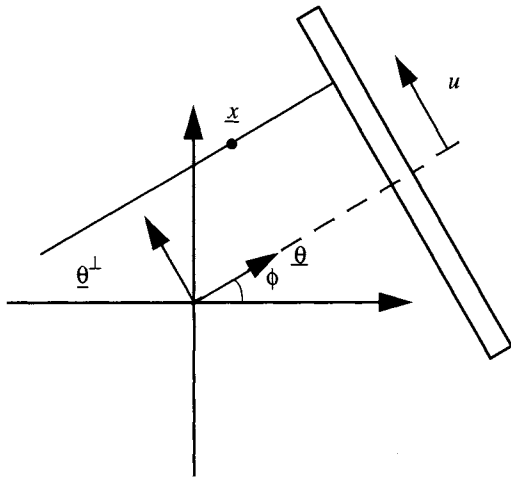


**FIGURE 6** The coordinate system used to describe parallel-beam projection data.

equal to the 2D image Fourier transform evaluated along the line through the origin in the direction  $\phi + \pi/2$ , i.e.:

$$\begin{aligned} G(U, \phi) &= \int_{-\infty}^{\infty} g(u, \phi) e^{-juU} du = F(X)|_{X=U\theta^\perp} \\ &= F(-U \sin \phi, U \cos \phi) \end{aligned} \quad (4)$$

where  $F(X) = F(X, Y)$  is the 2D image Fourier transform

$$\begin{aligned} F(X) &= F(X, Y) = \int_{-\infty}^{\infty} \int_{-\infty}^{\infty} f(x, y) e^{-jxX} e^{-jyY} dx dy \\ &= \iint_{R^2} f(x) e^{-j(X \cdot x)} dx \end{aligned} \quad (5)$$

This result, illustrated in Fig. 7, can be employed in a number of ways. The discrete Fourier transform (DFT, see

Chapter 2.3) of the samples of each 1D projection can be used to compute approximate values of the image Fourier transform. If the angular projection spacing is  $\Delta\phi$ , then the DFTs of all projections will produce samples of the 2D image Fourier transform on a polar sampling grid. The samples' loci lie at the intersections of radial lines, spaced by  $\Delta\phi$ , with circles of radii equal to integer multiples of the DFT frequency sampling interval. Once these samples are computed, the image can be reconstructed by first interpolating these values onto a regular Cartesian grid, and then applying an inverse 2D DFT. Design of these Fourier reconstruction methods involves a trade-off between computational complexity and accuracy of the interpolating function [4].

A more elegant solution can be found by re-working (4) into a spatial domain representation. It is then straightforward to show that the image can be recovered using the following equations [11]:

$$f(x) = \frac{1}{2} \int_0^{2\pi} \tilde{g}(u, \phi) \big|_{u=u_{x,\phi}} d\phi \quad (6)$$

where

$$\tilde{g}(u, \phi) = \frac{1}{4\pi^2} \int_{-\infty}^{\infty} G(U, \phi) |U| e^{juU} dU \quad (7)$$

and  $u_{x,\phi} = x \cdot \theta^\perp$  is the  $u$ -value of the parallel projection at angle  $\phi$  of the point  $x$ , see Fig. 6.

These two equations form the basis of the widely used filtered backprojection algorithm. Equation (7) is a linear shift-invariant filtering of the projection data with a filter with frequency response  $H(U) = |U|$ . The gain of this filter increases monotonically with frequency and the reconstruction is therefore unstable. However, by assuming that the data  $g(u, \phi)$ , and hence the corresponding image, are bandlimited

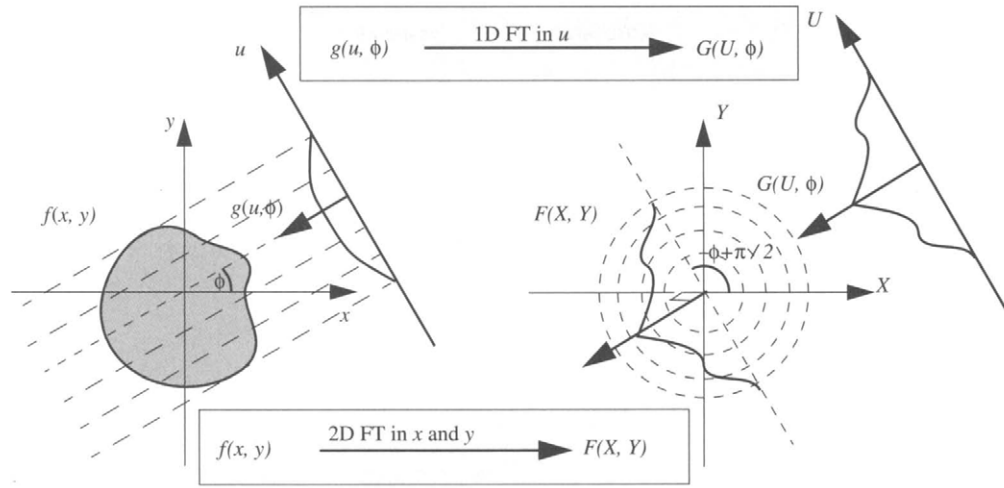


**FIGURE 7** Illustration of the projection slice theorem. The 2D image at left is projected at angle  $\phi$  to produce the 1D projection  $g(u, \phi)$ . The 1D Fourier transform,  $G(U, \phi)$  of this projection is equal to the 2D image Fourier transform,  $F(X, Y)$  along the radial line at angle  $\phi + \pi/2$ .

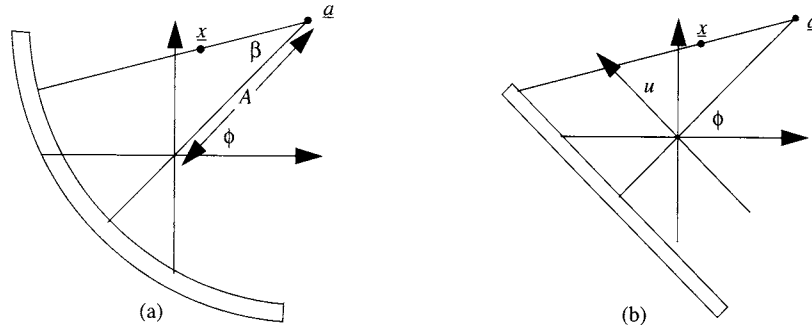


**FIGURE 8** Illustration of the coordinate system for fan-beam tomography using (a) circular arc and (b) linear detector array arrangements.

to a maximum frequency  $U = U_{max}$  we need only consider the finite bandwidth filter with impulse response:

$$h(u) = \int_{-U_{max}}^{U_{max}} |U| e^{juU} dU \quad (8)$$

The filtered projections  $\tilde{g}(u, \phi)$  are found by convolving  $g(u, \phi)$  with  $h(u)$  scaled by  $1/4\pi^2$ . To reduce effects of noise in the data, the response of this filter can be tapered off at higher frequencies [4, 11].

The integrand  $\tilde{g}(u, \phi)$  in (6) can be viewed as an image with constant values along lines in the direction that is formed by “backprojecting” the filtered projection at angle  $\phi$ . Summing (or in the limit, integrating) these backprojected images for all  $\phi$  produces the reconstructed image. Although this summation involves  $\phi \in [0, 2\pi]$ , in practice only 180 degrees of projection measurements are collected because opposing parallel-beam projections contain identical information. In (6), the integration limits can be replaced with  $\phi \in [0, \pi]$  and the factor of  $1/2$  can be removed. This filtered

backprojection method, or the modification described below for the fanbeam geometry, was the basis for image reconstruction in almost all commercially available computed tomography systems, at least until the end of the twentieth century.

### 3.2 Fan-Beam Filtered Backprojection

X-ray CT data can be collected more rapidly using an array of detectors and a fan-beam x-ray source so that all elements in the array are simultaneously exposed to the x-rays. This arrangement gives rise to a natural fan-beam data collection geometry as illustrated in Fig. 1b. The source and detector array are rotated around the patient and a set of fan-beam projections,  $g(a, \theta)$ , are collected, where  $a$  represents the position of the source and  $\theta$  specifies the individual line integrals in the projections. For a radius of rotation  $A$ , we parametrize the motion of the source as  $a = (A \cos \phi, A \sin \phi)$ . For the case of a circular arc of detectors whose center is the fan-source and which rotates with the source, a particular detector element is conveniently specified using the relative angle  $\beta$  as shown in Fig. 8a. The fan-beam projection notation

is then simplified to  $g(\phi, \beta) = g(a, \theta) = \int f(a + t\theta)dt$  where  $\theta = (-\cos(\phi - \beta), -\sin(\phi - \beta))$ .

The projection data could be re-sorted into equivalent parallel projections and the above reconstruction methods applied. Fortunately, this re-sorting is unnecessary. It can be shown [12] that reconstruction of the image can be performed using a fan-beam version of the filtered back-projection method. Development of this inverse method involves substitution of the fan-beam data in the parallel-beam formulae, (6) and (7), and applying a change of variables with the appropriate Jacobian. After some manipulation, the equations can be reduced to the form:

$$f(x) = \frac{1}{2} \int_0^{2\pi} \frac{1}{r^2} \tilde{g}(\phi, \beta) \Big|_{\beta=\beta_{x,\phi}} d\phi \quad (9)$$

where  $r = \|x - a\|$  is the distance from the point  $x$  to the fan-beam source,

$$\tilde{g}(\phi, \beta) = \frac{1}{4\pi^2} \int_{-\gamma}^{\gamma} (A \cos \beta' g(\phi, \beta')) h(\sin(\beta - \beta')) d\beta' \quad (10)$$

and  $\gamma$  is the maximum value of  $\beta$  required to ensure that data are not truncated. In (9),  $\beta_{x,\phi} = \cos^{-1}((A^2 - (x \cdot a))/(rA))$  indicates the value in the  $\phi$ -projection for the line passing through the point  $x$ .

As in the parallel-beam case, this reconstruction method involves a two step procedure: filtering, in this case with a pre-weighting factor  $A \cos \beta$ , and backprojection. The back-projection for fan-beam data is performed along the paths converging at the location of the x-ray source and includes an inverse square-distance weighting factor. The filter  $h(u)$  was given in (8) and, as before, can include a smoothing window tailored to the expected noise in the measured data.

In some fan-beam tomography applications the detector bank might be linear rather than curved. In principle, the same formula could be used by interpolating to obtain values sampled evenly in  $\beta$ . However, there is an alternative formula suitable for linear detectors. In this case we use  $u$  to indicate the projection line for a scaled version of the flat detector corresponding to a virtual flat detector passing through the origin as shown in Fig. 8b. The simplified notation is  $g(\phi, u) = g(a, \theta) = \int f(a + t\theta)dt$  where  $a = (A \cos \phi, A \sin \phi)$  as before, and  $\theta = (u \sin \phi - A \cos \phi, -u \cos \phi - A \sin \phi) / \sqrt{u^2 + A^2}$ .

The derivation of the fan-beam formula for linear detectors is virtually the same as for the curved detectors, and results in equations of the form:

$$f(x) = \frac{1}{2} \int_0^{2\pi} \left( \frac{A^2 + u^2}{r^2} \tilde{g}(a, u) \right) \Big|_{u=u_{x,\phi}} d\phi \quad (11)$$

$$\tilde{g}(a, u) = \frac{1}{4\pi^2} \int_{-\infty}^{\infty} \left( \frac{A}{\sqrt{A^2 + u'^2}} g(a, u') \right) h(u - u') du' \quad (12)$$

where, as before,  $r = \|x - a\|$  is the distance between  $x$  and the source point  $a$ , and  $u_{x,\phi} = A \tan \beta$  specifies the line passing through  $x$  in the  $\phi$  projection. The limits of integration  $[-\infty, \infty]$  in the filtering step (12) are replaced in practice with the finite range of  $u$  corresponding to non-zero values of the projection data  $g(u, \phi)$ .

The existence of a filtered backprojection algorithm for these two fan-beam geometries is quite fortuitous, and does not occur for all detector sampling schemes. In fact these are two of only four sampling arrangements that admit this convenient reconstruction form [13]. In general, the filtering step must be replaced with a more general linear operation on the weighted projection values, and results in a more computationally intensive algorithm.

For the fan-beam geometry, opposing projections do not contain the same information, although all line integrals are measured twice over the range of  $2\pi$  measurements. The redundancy is interwoven in the projections. An angular range of  $\pi + \gamma$  can be used with careful adjustments to (11) and (12) to obtain a fast "short scan" reconstruction [4]. These short scan modes are used in clinical CT systems including spiral CT systems as discussed in Section 4.2.

Important new developments in fan-beam image reconstruction occurred at the turn of the century. New image reconstruction formulas were established that admitted partial reconstruction of the object if less than a short scan of fan-beam measurements had been collected. Observe from (11) and (12) that reconstruction at the point  $x$  uses all the data, namely all lines passing through the image. From these formulas it is not possible to obtain even a partial image if some of the data are missing. The new image reconstruction formulae are able to recover part of the image, often referred to as a *region of interest*, from part of the data. For fan-beam scanning with a contiguous circular motion of the source, any region of interest inside the convex hull of the source trajectory can be recovered using these formulae. For non-contiguous trajectories and for non-circular motions the description of which regions of interest are recoverable is more complicated [14].

These developments in fan-beam reconstruction have ignited new research into parallel beam reconstruction methods. Full  $180^\circ$  coverage is still required in parallel beam geometries even for region of interest reconstruction, but when the new fan-beam formulae are converted back to parallel beam, they provide methods of accurately handling truncated projections. Novel reconstruction formulae distinct from (6) and (7) have been established, and investigation is underway to determine the relationship between a desired region of interest and which subsets of the measured data are sufficient for accurate reconstruction [15].



## 4 Extending 2D Methods into 3D

### 4.1 Extracting 2D Data from 3D

A full 3D image can be built up by repeatedly performing 2D image reconstruction on a set of parallel contiguous slices. In x-ray CT, SPECT, and PET, this has been a standard method for volume tomographic reconstruction. Mathematically we use  $f_z(x) = f_z(x, y)$  to represent the z-slice of  $f(x, y, z)$ , and  $g_z(u, \theta)$  to represent the line integrals in this z-slice. Reconstruction for each  $z$  is performed sequentially using techniques described in Section 3.

More sophisticated methods of building 3D tomographic images have been developed for a number of applications. For example, in spiral x-ray CT, the patient is moved continuously through the scanner so no fixed discrete set of tomographic slices is defined. In this case there is flexibility in choosing the slice spacing and the absolute slice location, however, there is no slice position for which a complete set of projection data is measured. We describe image reconstruction for spiral CT in Section 4.2.

In a more general framework, we call an image reconstruction problem *fully 3D* if the data cannot be separated into a set of parallel contiguous and independent 2D slices. An example is 3D PET which allows measurement of oblique coincidence events and therefore must handle lineintegrals that cross multiple transverse planes as shown in Fig. 3c. Other examples of fully 3D problems include cone-beam SPECT and cone-beam x-ray CT where the diverging geometry of the rays precludes any sorting arrangement into parallel planes. Fully 3D image reconstruction is described in more detail in Section 5, but a common feature of these methods is the heavy computational load associated with the 3D backprojection step. Since 2D reconstruction is generally very fast, a number of approaches reduce computation cost by converting a fully 3D problem into a multi-slice 2D problem. These *rebinning* procedures involve approximations that in some instances are very good so significant improvements in

image reconstruction time can be achieved with little resolution loss. One such example is the Fourier Rebinning (FORE) method used in 3D PET imaging where an order of magnitude improvement in computation time is achieved over the standard fully 3D methods; the method is described in Section 4.3.

### 4.2 Spiral CT

In spiral CT a conventional fan-beam x-ray source and detector system rotates around the patient while the bed is translated along its long axis, as illustrated in Fig. 9. This supplementary motion, although it complicates the image reconstruction algorithms and results in slightly blurred images, provides the capability to scan large regions of the patient in a single breath hold.

The helical motion is characterized by the pitch  $P$  which is the amount of translation in the axial or  $z$ -direction for a full rotation of the source and detector assembly. Therefore  $\phi = 2\pi z/P$  and we can write  $g(z, \beta) = g(a, \theta) = \int f(a + t\theta) dt$  which is similar to the fan-beam geometry of Section 3.2, with  $a = (A \cos \phi, A \sin \phi, z)$  and  $\theta = (-\cos(\phi - \beta), -\sin(\phi - \beta), 0)$ . Note that  $\phi$  now ranges from 0 to  $2\pi n$ , as  $z$  ranges from 0 to  $nP$  where  $n$  is the number of turns of the helix. The usual method of reconstruction involves estimating a full set of fan-beam projections  $g_z(\phi, \beta)$  for each transverse plane, using the available projections at other points on the helix. If the reconstruction on transverse plane  $z$  is required, the standard fan-beam CT algorithm is used,

$$f_z(x) = \frac{1}{2} \int_0^{2\pi} \frac{1}{r^2} \tilde{g}_z(\phi, \beta) \Big|_{\beta=\beta_{z,x,\phi}} d\phi \quad (13)$$

$$\tilde{g}_z(\phi, \beta) = \frac{1}{4\pi^2} \int_{-\gamma}^{\gamma} (A \cos \beta' g_z(\phi, \beta')) h(\sin(\beta - \beta')) d\beta' \quad (14)$$

where  $\beta_{z,x,\phi}$  indicates the relative projection angle  $\beta$  found by projecting in the  $z$  plane at angle  $\phi$  through the point  $(x, y, z)$ ,

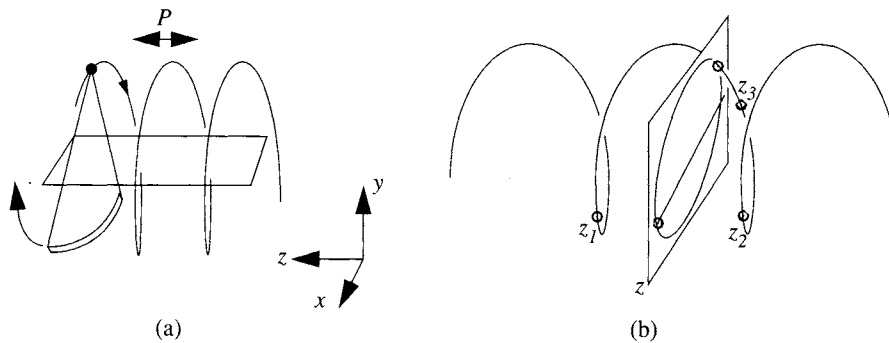


**FIGURE 9** Illustration of spiral or helical CT geometry. (a) Relative to a stationary bed, the source and detector circle the patient in a helical fashion with pitch  $P$ ; (b) to reconstruct cross section  $f_z(x, y)$  missing projections are interpolated from neighboring points on the helix at which data were collected.

and  $r$  is the distance (in the  $z$  plane) between the point  $(x, y, z)$  and the virtual source at angular position  $\phi$ . In the simplest case, the  $z$ -plane projections  $g_z(\phi, \beta)$  are estimated by a weighted sum of the measured projections at the same angular position above and below  $z$  on the helix:

$$g_z(\phi, \beta) \approx \frac{w_1 g(z_1, \beta) + w_2 g(z_2, \beta)}{w_1 + w_2} \quad (15)$$

for some suitable weights  $w_1$  and  $w_2$ , and where, as illustrated in Fig. 9,  $z_1$  and  $z_2$  lie within one pitch  $P$  of the reconstruction plane,  $z$ . Note that in (15),  $z_1/P$  differs from  $\phi$  by some multiple of  $2\pi$ , and similarly for  $z_2$ .

Various schemes for choosing the weights  $w_1$  and  $w_2$  exist [16]. Each weighting scheme establishes a trade-off between increased image noise from unbalanced contributions, and inherent axial blurring artifacts from the geometric approximation of the estimation process. When the image noise is particularly low, a short-scan version of the fan-beam reconstruction algorithm might be used. This version reduces the range of contributing projections to  $\pi + \gamma$  from  $2\pi$  and correspondingly reduces the maximum distance required to estimate a projection  $g_z(\phi, \beta)$ . Even more elaborate estimation schemes exist, such as approximating  $g_z(\phi, \beta)$  on a line-by-line basis. Figure 9b illustrates how the line-integral  $g_z(\phi, \beta)$  could be estimated from a value in the  $z_3$  projection.

The choice of pitch  $P$  represents a compromise between maximizing the axial coverage of the patient, and avoiding unacceptable artifacts from the geometric estimation. Generally the pitch is chosen between one and two times the thickness of the detector in the axial direction [16].

In recent years, “multi-slice” CT scanners have been constructed with multiple rows of detectors. For four detector rows or less, the typical approach has been to ignore the divergence of the rays in the axial direction and treat the system as several interwoven helices, so that the methods described above can be applied. The pitch is usually tunable, and does not normally exceed the axial extent of the detectors. However, newer systems with a greater number of detector rows involve a non-negligible axial divergence of the x-rays and need to be treated using cone-beam techniques to correctly handle the divergence issue. Section 5.2 describes cone-beam tomography in general and briefly discusses the situation for spiral (or helical) CT.

### 4.3 Rebinning Methods in 3D PET

PET data is generally sorted into parallel-beam projections,  $g(u, \phi)$  as described in Section 3.1. For a multi-ring 2D PET scanner the data are usually processed slice-by-slice. Using  $z$  to denote the axis of the scanner, the data are reconstructed

using (6) and (7) applied to each  $z$ -slice as follows:

$$f_z(x) = \frac{1}{2} \int_0^{2\pi} \tilde{g}_z(u, \phi) \big|_{u=u_{z,x,\phi}} d\phi \quad (16)$$

$$\tilde{g}_z(u, \phi) = \frac{1}{4\pi^2} \int_{-\infty}^{\infty} g_z(u', \phi) h(u - u') du \quad (17)$$

with  $u_{z,x,\phi} = (x, y, z) \cdot (-\sin \phi, \cos \phi, 0)$ . The data  $g_z(u, \phi)$  are found from sampled values of  $u$  and  $\phi$  determined by the ring geometry: the radius  $R$  and the number of crystals (typically several hundreds). In (16) and (17),  $z$  is usually chosen to match the center of each detector ring. In practice, 2D scanners do allow detection of coincidences between adjacent rings. By using the singleslice rebinning (SSRB) technique described below, slices midway between adjacent detector rings can also be reconstructed from 2D scanner data.

Current commercial 3D PET scanners usually consist of a few tens of detectors rings and have the capability to detect oblique photon pairs that strike detectors in different rings. These fully 3D data require more advanced reconstruction techniques. The fully 3D version of (16) and (17) is given in Section 5. In this section we describe two popular rebinning methods, where the data are first processed to form independent 2D projections  $g_z(u, \phi)$  from which (16) and (17) are then used for image reconstruction.

Let  $\Delta$  denote the spacing between rings. Let  $g_{l,m}(u, \phi)$  denote the resulting line-integral, with endpoints on rings  $l$  and  $m$ , whose 2D projection variables are  $(u, \phi)$  when the line is projected onto the  $x$ - $y$  plane, as shown in Fig. 10. In the SSRB method [17], all line-integral data are reassigned to the slice midway between the rings where the detection occurred. Thus

$$g_z(u, \phi) \approx \sum_{(l,m) \in \Omega_z} g_{l,m}(u, \phi) \quad \text{where} \quad (18)$$

$$\Omega_z = \left\{ (l, m) : \frac{(l+m)\Delta}{2} = z \right\}$$

and reconstruction proceeds according to (16) and (17).

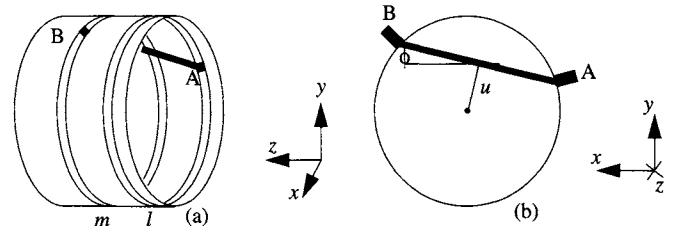


FIGURE 10 Oblique line integrals (along the path AB in (a)) between different rings of detectors can be rebinned into equivalent in plane data either directly using SSRB, or indirectly using FORE. (b) The relationship between the projected line integral path and the parameters  $(u, \phi)$ .

A more sophisticated method, known as Fourier Rebinning (FORE) [18], effectively performs the rebinning operation in the 2D frequency domain. The rebinned data  $g_z(u, \phi)$  are found using the following transformations:

$$\tilde{g}_{l,m}(u, \phi) = g_{l,m}(u, \phi) \frac{2\sqrt{R^2 - u^2}}{\sqrt{4R^2 - 4u^2 + (l-m)^2 \Delta^2}} \quad (19)$$

$$\tilde{G}_{l,m}(U, k_\phi) = \int_{-\infty}^{\infty} \int_0^{2\pi} \tilde{g}_{l,m}(u, \phi) e^{-j(Uu + k_\phi \phi)} d\phi du \quad (20)$$

$$G_z(U, k_\phi) \approx \sum_{(l,m) \in \Omega_z} \tilde{G}_{l,m}(U, k_\phi) \quad (21)$$

$$\text{where } \Omega_z = \left\{ l, m : \frac{(l+m)\Delta}{2} + \frac{(l-m)\Delta}{2} \frac{k_\phi}{U\sqrt{R^2 - U^2}} = z \right\} \quad (22)$$

$$g_z(u, \phi) = \sum_{k_\phi} \int_{-\infty}^{\infty} G_z(U, k_\phi) e^{j(Uu + K_\phi \phi)} dU \quad (23)$$

Both SSRB and FORE are approximate techniques and the geometric misplacement of the data can cause artifacts in the reconstructed images. However, FORE is far more accurate than SSRB yet almost as fast computationally (compared to the subsequent reconstruction time using (16) and (17)). In [18] a mathematically exact rebinning formula is presented and it is shown that SSRB and FORE represent zeroth and first order versions of this formula. However, algorithms using the exact version are less practical than SSRB or FORE.

Image reconstruction can be performed using a 3D version of the filtered backprojection formulas (6) and (7) given in Section 3.1:

$$f(x) = \frac{1}{2} \int_{\Omega} \tilde{g}(u, v, \theta) \Big|_{\substack{u=u_{x,\theta} \\ v=v_{x,\theta}}} d\theta \quad (24)$$

$$\tilde{g}(u, v, \theta) = \frac{1}{8\pi^3} \int_{-\infty}^{\infty} \int_{-\infty}^{\infty} G(U, V, \theta) H_{\Omega}(U, V, \theta) e^{j(uU + vV)} dU dV \quad (25)$$

where, in the surface integral of (23),  $d\theta$  can be written as  $\sin \theta d\theta d\phi$  for  $\theta$  having polar angle  $\theta$  and azimuthal angle  $\phi$ ; and where  $(u_{x,\theta}, v_{x,\theta}) = (x \cdot \theta^1, x \cdot \theta^2)$  represents the  $(u, v)$  coordinates of the line with orientation  $\theta$  passing through  $x$ . The subset  $\Omega$  of the unit sphere represents the measured directions  $\{\theta\}$  and must satisfy Orlov's condition for data completeness in order for (24) and (25) to be valid. Orlov's condition requires that every great circle on the unit sphere intersect the region  $\Omega$ . The tomographic reconstruction filter  $H_{\Omega}(U, V, \theta)$  depends on the measured data set [19]. In the special case that  $\Omega$  is the whole sphere  $S^2$ , then  $H_{\Omega}(U, V, \theta) = \sqrt{U^2 + V^2}$ .

In 3D PET imaging, data can be sorted according to the parameterization  $g(u, v, \theta)$ . The set of measured projections can be described by  $\Omega_{\Psi} = \{\theta = (\theta_x, \theta_y, \theta_z) : |\theta_z| \leq \sin \Psi\}$  where  $\Psi$  represents the most oblique line integral possible,  $\Psi = \text{atan}(L/(2R))$ , for a scanner radius of  $R$  and axial extent  $L$ . Provided none of the projections are truncated, reconstruction can be performed according to (23) and (24) using the Colsher filter  $H_{\Omega_{\Psi}}(U, V, \theta) = H^{\Psi}(U, V, \theta)$  given by

$$H^{\Psi}(U, V, \theta) = \begin{cases} \sqrt{U^2 + V^2} & \text{if } \sqrt{U^2 + \theta_z^2 V^2} < (\sin \Psi) \sqrt{U^2 + V^2} \\ \frac{\pi}{2 \sin^{-1}((\sin \Psi) \sqrt{U^2 + V^2} / \sqrt{U^2 + \theta_z^2 V^2})} \sqrt{U^2 + V^2} & \text{otherwise} \end{cases} \quad (26)$$

## 5 3D Image Reconstruction

### 5.1 Fully 3D Reconstruction with Missing Data

In 3D image reconstruction, parallel-beam projection data can be specified using  $\theta$ , the direction of the line integrals, and two scalars  $(u, v)$  that indicate offsets in directions  $\theta^1$  and  $\theta^2$  perpendicular to  $\theta$ . Therefore  $g(u, v, \theta) = g(a, \theta) = \int f(a + t\theta) dt$  where  $a = u\theta^1 + v\theta^2$ , and  $\{\theta, \theta^1, \theta^2\}$  is an orthonormal system. Note that all vectors in this section are 3D.

In practice the object occupies most of the axial extent of the scanner so nearly all projections are truncated. However, there is always a subset  $\Omega_{\Psi'}$  of the projections which are not truncated, and from these projections a reconstruction can be performed to obtain the image  $f^{\Psi'}(x)$  using (25) and (26) with  $H^{\Psi'}(U, V, \theta)$ . In the absence of noise, this reconstruction would be sufficient, but to include the partially measured projections a technique known as the "reprojection method" is used. All truncated projections are completed by estimating the missing line integrals based on the initial reconstruction  $f^{\Psi'}(x)$ . Then, in a second step, reconstruction from the entire

data set is performed using  $H^\Psi(U, V, \theta)$  to obtain the final image  $f^\Psi(x)$  [20].

## 5.2 Cone-Beam Tomography

For cone-beam projections it is convenient to use the general notation  $g(a, \theta)$  where  $a$  and  $\theta$  are three-dimensional vectors. For an x-ray system, the position of the source would be represented by  $a$  and the direction of individual ray-sums obtained from that source would be indicated by  $\theta$ . Due to difficulties obtaining sufficient tomographic data (see below), the source and/or detector may follow elaborate trajectories in space relative to the object; therefore a general description of their orientations is required. For applications involving a planar detector, we replace  $\theta$  with,  $(u, v)$  coordinates on an imaginary detector centered at the origin and lying in the plane perpendicular to  $a$ . The source point  $a$  is assumed never to lie on the scanner axis  $e_3$ . The  $u$ -axis lies in the detector plane in the direction  $e_3 \times a$ . The  $v$ -direction is perpendicular to  $u$  and points in the same direction as  $e_3$  as shown in Fig. 11b.

In the simplest applications, the detector and source rotate in a circle about the scanner axis  $e_3$ . If the radius of rotation is  $A$ , the source trajectory is parameterized by  $\phi \in [0, 2\pi]$  as  $a = (A \cos \phi, A \sin \phi, 0)$ . In this case the  $v$  axis in the detector stays aligned with  $e_3$  and the  $u$  axis points in the tangent direction to the motion of the source. Physical detector measurements can easily be scaled to this virtual detector system, just as for the fan-beam example of Section 3.2. Thus  $g(\phi, u, v) = g(a, \theta) = \int f(a + t\theta) dt$  where  $\theta = (-u \sin \phi - A \cos \phi, u \cos \phi - A \sin \phi, v)$ .

The algorithm of Feldkamp et al. [21] is based on the fan-beam formula for flat detectors (see Section 3.2) and collapses to this formula in the central plane  $z = 0$  where only

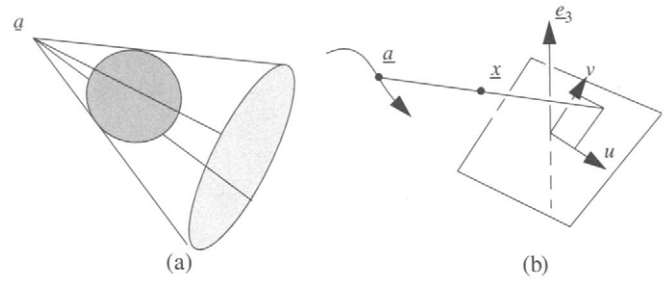


**FIGURE 11** (a) 2D planar projections of a 3D object are collected in a cone-beam system as line integrals through the object from the cone vertex  $a$  to the detector. (b) The coordinator system for the cone-beam geometry—the cone vertices  $a$  can follow an arbitrary trajectory provided Tuy's condition is satisfied.

fan-beam measurements are taken.

$$f_{\text{FDK}}(x) = \frac{1}{2} \int_0^{2\pi} \left( \frac{A^2 + u^2 + v^2}{r^2} \tilde{g}(\phi, u, v) \right) \bigg|_{u=u_{x,\phi}}^{u=u_{x,\phi}} \bigg|_{v=v_{x,\phi}}^{v=v_{x,\phi}} d\phi \quad (27)$$

$$\tilde{g}(\phi, u, v) = \frac{1}{4\pi^2} \int_{-\infty}^{\infty} \left( \frac{A}{\sqrt{A^2 + u'^2 + v'^2}} g(\phi, u', v') \right) h(u - u') du' \quad (28)$$

Similarly to (11),  $r = \|x - a\|$  is the distance between  $x$  and the source position  $a$ , and  $(u_{x,\phi}, v_{x,\phi})$  are the coordinates on the detector of the cone-beam projection of  $x$ , see Fig. 11. Figure 12 shows two images of reconstructions from mathematically simulated data. Using a magnified grayscale to reveal the 1% contrast structures, the top images show both a high quality reconstruction in the horizontal transverse slice at the level of the circular trajectory, and apparent decreased intensity on planes above and below this level. These artifacts

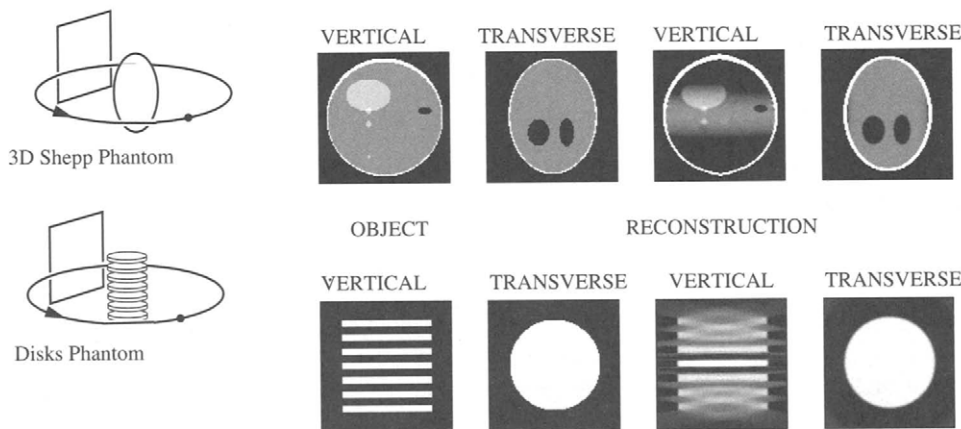


**FIGURE 12** Example of cone-beam reconstructions from a circular orbit—the obvious artifacts are a result of the incompleteness in the data. Other trajectories, such as a helix or a circle plus line, give complete data and artifact free reconstructions.

are characteristic of the Feldkamp algorithm. The bottom images, showing reconstructions for the “disks” phantom, also exhibit cross-talk between transverse planes and some other less dramatic artifacts. The disks phantom is specifically designed to illustrate the difficulty in using cone-beam measurements for a circular trajectory. Frequencies along and near the scanner axis are not measured, and objects with high amplitudes in this direction produce poor reconstructions.

For the cone-beam configuration, requirements for a tomographically complete set of measurements are known as Tuy’s condition. Tuy’s condition is expressed in terms of a geometric relationship amongst the trajectory of the cone-beam vertex point (the source point) and the size and position of the object being scanned. Tuy’s condition requires that every plane that cuts through the object must also contain some point of the vertex trajectory. Furthermore, it is assumed that the detector is large enough to measure the entire object at all positions of the trajectory, i.e., the projections should not be truncated. For the examples given in Fig. 12, the artifacts arose because the circular trajectory did not satisfy Tuy’s condition (even though the projections were not truncated). In this sense the measurements were incomplete and artifacts were inevitable.

Analytic reconstruction methods for cone-beam configurations satisfying Tuy’s completeness condition are generally based on a transform pair that plays a similar role to the Fourier transform in the projection slice theorem for classic parallel-beam tomography. A mathematic result due to Grangeat [22] links the information in a single cone-beam projection to a subset of the transform domain, just as the Fourier slice theorem links a parallel projection to a certain subset of the Fourier domain. This relationship is defined through the “ $B$  transform”, the derivative of the 3D Radon transform:

$$Bf(s, \gamma) = p(s, \gamma) = \frac{1}{2\pi} \int_{R^3} f(x) \delta'(x \cdot \gamma - s) dx \quad (29)$$

$$B^{-1}p(x) = f(x) = \frac{1}{4\pi} \int_{S^2} \int_R p(s, \gamma) \delta'(s - x \cdot \gamma) ds d\gamma \quad (30)$$

where  $s$  is a scalar and  $\|\gamma\| = 1$ . The symbol  $\delta'$  represents the derivative of the Dirac delta function whose action is defined by  $\int_{-\infty}^{\infty} f(s) \delta'(s_0 - s) ds = f'(s_0)$ .

Grangeat’s formula can be written

$$\frac{1}{4\pi} \int_{S^2} g(a, \theta) \delta'(\theta \cdot \gamma) d\theta = p(s, \gamma)|_{s=a \cdot \gamma} \quad (31)$$

An analysis of (31) shows that if Tuy’s condition is satisfied, then all values are available in the  $B$  domain representation of  $f(x)$ , namely  $p(s, \gamma)$  [22].

Equations (30) and (31) form the basis for a reconstruction algorithm. All values in the  $B$  domain can be found from cone-beam projections, and  $f(x)$  can be recovered from the inverse transform  $B^{-1}$ . Care must be taken to ensure that the  $B$  domain is sampled uniformly in  $s$  and  $\gamma$ , and that if two different cone-beam projections provide the same value of  $p(s, \gamma)$  the contributions must be normalized. The method follows the concept of direct Fourier reconstruction described in Section 3.1.

A filtered backprojection type of formulation for cone-beam reconstruction is also possible, see, for example, [23]. If the trajectory is a piecewise smooth path, parameterized mathematically by  $\phi \in \Phi \subset R$ , a reconstruction formula similar to filtered backprojection can be derived from equations (30) and (31):

$$f(x) = \frac{1}{2} \int_{\Phi} \frac{\tilde{g}(a(\phi), \theta)}{r^2} \Big|_{\theta=\theta_{x,\phi}} d\phi \quad (32)$$

$$\begin{aligned} \tilde{g}(a(\phi), \theta) = & \frac{-1}{8\pi^2} \int_{S^2} \left( \int_{S^2} f(a(\phi), \theta') \delta'(\theta' \cdot \gamma) d\theta' \right) \\ & \times \delta'(\theta \cdot \gamma) M(\gamma, \phi) |a'(\phi) \cdot \gamma| d\gamma \end{aligned} \quad (33)$$

Here  $r = \|x - a(\phi)\|$ ,  $\theta_{x,\phi} = (x - a(\phi))/\|x - a(\phi)\|$  is the line passing through  $x$  for the  $a(\phi)$  projection, and the function  $M$  must be chosen to normalize multiple contributions in the  $B$  domain [23]. The normalization condition is  $1 = \sum_{k=1}^{n(\gamma,s)} M(\gamma, \phi_k)$  where  $n(\gamma, s)$  is the number of vertices lying in the plane with unit normal  $\gamma$  and displacement  $s$ , and  $\phi_1, \phi_2, \dots, \phi_{n(\gamma,s)}$  indicate the vertex locations where the path  $a(\Phi)$  intersects the plane. By Tuy’s condition, for  $n(\gamma, s) > 0$  for  $|s| < R$ .

These equations must be tailored to the specific application. When the variables are changed to reflect the planar detector arrangement specified at the beginning of this subsection, the above equations resemble the Feldkamp algorithm with a much more complicated “filtering” step. To simplify notation, we write  $A$  for the varying distance  $\|a(\phi)\|$  of the vertex from the origin.

$$f(x) = \frac{1}{2} \int_{\Phi} \left( \frac{A^2 + u^2 + v^2}{r^2} \tilde{g}(a(\phi), u, v) \right) \Big|_{\substack{u=u_{x,\phi} \\ v=v_{x,\phi}}} d\phi \quad (34)$$

$$\begin{aligned} \tilde{g}(a(\phi), u, v) = & \frac{-1}{4\pi^2} \int_0^\pi \left( \frac{d}{dt} T(\phi, \gamma) \frac{\sqrt{A^2 + t^2}}{A^2} \right. \\ & \times \left. \left( \frac{d}{dt} \int_R \frac{A}{\sqrt{A^2 + u'^2 + v'^2}} g(a, u', v') dl \right) \right) \Big|_{\substack{t=u \cos \mu \\ + v \sin \mu}} d\mu \end{aligned} \quad (35)$$

where, in the innermost integration,  $(u', v') = (t \cos \mu - l \sin \mu, t \sin \mu + l \cos \mu)$ ; the function  $T(\phi, \gamma) = |a'(\phi) \cdot \gamma| M(\gamma, \phi)$  contains all the dependency on the particular trajectory. Note that in (35),  $\gamma = (A \cos \mu e_u + A \sin \mu e_v + t e_w) / (\sqrt{A^2 + t^2})$  where the detector coordinate axes are  $e_u$  and  $e_v$ , and  $e_w = -a(\phi)/A$ .

Although these equations are only valid when the cone-beam configuration satisfies Tuy's condition, the algorithm of equations (34) and (35) collapses to the Feldkamp algorithm when a circular trajectory is specified. This general algorithm has been refined and tailored for specific applications involving truncated projections. Practical methods have been published for the case of source trajectories containing a circle.

The case of a helical trajectory is particularly important for the latest generation of CT scanners with many detector rows. The framework of (32) and (33) does not apply directly to helical CT scanning because the projections in any practical CT scanner will always be truncated in the axial direction. Furthermore, different segments of the helical trajectory are used to reconstruction different parts of the patient. The methods used to treat these problems appeal to specific properties of the helical trajectory, such as the PI-line, which is the unique line passing through a specified point in the image and connecting two trajectory points within a single turn of the helix. Using these properties, recent theoretical developments in helical image reconstruction are being described in a framework similar to (32) and (33), with careful choices for the function  $M$ . The goal of helical cone-beam image reconstruction is to find a fast, accurate filtered backprojection algorithm that can handle the axial truncation with the minimum detector usage yet with the flexibility to incorporate redundant information when a small pitch is used for improved signal to noise ratios in the images.

## 6 Iterative Reconstruction Methods

### 6.1 Finite Dimensional Formulations and ART

As noted above, the line-integral model on which all of the preceding methods are based is only approximate. Furthermore, there is no explicit modeling of noise in these approaches; noise in the data is typically reduced by tapering off the response of the projection filters before backprojection. In x-ray CT, the beam is highly collimated, the detectors are high resolution and the number of photons per measurement is very large; consequently the line integral approximation is adequate to produce low noise images at sub-millimeter resolution in humans. However, this may not be the case in industrial and other non-medical applications, and these systems may benefit from more accurate modeling of the data and noise. In the case of PET and SPECT, the often low

intrinsic resolution of detectors, depth dependent and geometric resolution losses, and the typically low photon count, can lead to rather poor resolution at acceptable noise levels when using direct reconstruction methods. An alternative to the direct approach is to use a finite dimensional model in which the detection system and the noise statistics can be modeled more accurately. Research in this area has led to the development of a large class of reconstruction methods that often out-perform the direct methods.

We will assume that the image is adequately represented using a finite set of basis functions. While there has been some interest in alternative basis elements, almost all researchers currently use a cubic voxel basis function. Each voxel is an indicator function on a cubic region centered at one of the image sampling points in a regular 2D or 3D lattice. The image value at each voxel is proportional to the quantity being imaged integrated over the volume spanned by the voxel. To allow a unified treatment of 2D and 3D problems, a single index will be used to represent the lexicographically ordered elements of the image  $f = \{f_1, f_2, \dots, f_N\}$ . Similarly, the elements of the measured projections will be represented in lexicographically ordered form as  $y = \{y_1, y_2, \dots, y_M\}$ .

In x-ray CT we can model the attenuation of a finite width x-ray beam as the integral of the linear attenuation coefficient over the path (or strip) through which the beam passes. Thus the measurements can be written as:

$$y_i = \iint_{x, y \in \text{strip}(i)} f(x, y) dx dy = \sum_{j=1}^N H_{ij} f_j \quad (36)$$

where  $f_j$  is the attenuation coefficient at the  $j$ th voxel. The elements  $H(i, j)$  of the projection matrix  $H$  is equal to the area of intersection of the  $i$ th strip with the indicator function on the  $j$ th voxel, see Fig. 13. Equation (36) represents a huge

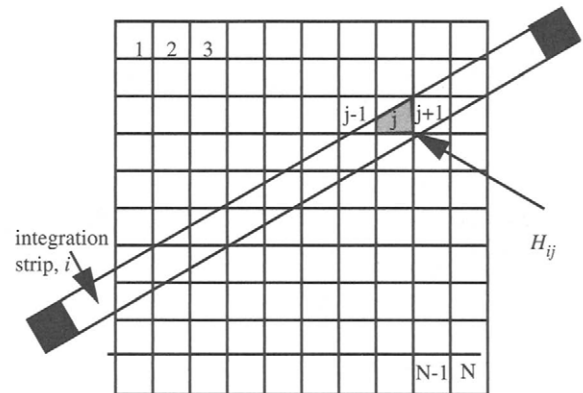


**FIGURE 13** Illustration of the pixel-based finite dimensional formulation used in iterative x-ray CT reconstruction. The matrix element  $H_{ij}$  gives the contribution of the  $j$ th voxel to the  $i$ th measurement and is proportional to the areas of intersection of the voxel with the strip that joins the source and detector.

set of simultaneous linear equations,  $\mathbf{y} = \mathbf{H}\mathbf{f}$ , that can be solved to compute the CT image  $\mathbf{f}$ . In principle the system can be solved using standard methods. However, the size of these systems coupled with the special structure of  $\mathbf{H}$  motivated research into more efficient specialized numeric procedures. These methods exploit the key property that  $\mathbf{H}$  is very sparse, i.e., most elements in the matrix are zero, since the path along which each integration is performed intersects only a small fraction of the image pixels.

One algorithm that makes good use of the sparseness property is the algebraic reconstruction technique or ART [24]. This method finds the solution to the set of equations in an iterative fashion through successive orthogonal projection of the current image estimate onto hyperplanes defined by each row of  $\mathbf{H}$ . If this procedure converges, the solution will be a point where all of the hyperplanes intersect, i.e., a solution to (36). Let  $\mathbf{f}^n$  represent the vector of image pixel values at the  $n$ th iteration, and let  $\mathbf{h}_i^T$  represent the  $i$ th row of  $\mathbf{H}$ . The ART method has the following form:

$$\mathbf{f}^{n+1} = \mathbf{f}^n + \left( \frac{y_i - \mathbf{h}_i^T \mathbf{f}^n}{\mathbf{h}_i^T \mathbf{h}_i} \right) \mathbf{h}_i \quad i = (n \bmod N) + 1 \quad (37)$$

ART can also be viewed in terms of the backprojection operator used in filtered backprojection: each iteration of (37) is equivalent to adding to the current image estimate  $\mathbf{f}^n$  the weighted backprojection of the error between the  $i$ th measured projection sample and the projection corresponding to  $\mathbf{f}^n$ . ART will converge to a solution of (36) provided the system of equations is consistent. In the inconsistent case, the iterations will not converge to a single solution and the properties of the image at a particular stopping point will be dependent on the sequence in which the data are ordered. Many variations of the ART method can be found in the literature. These variations exhibit differences in convergence behavior, sensitivity to noise, and optimality properties [25].

## 6.2 Statistical Formulations

The ART method does not directly consider the presence of noise in the data. While acceptable in high SNR x-ray CT data, the low photon counting statistics found in PET and SPECT should be explicitly considered. The finite dimensional formulation in Section 6.1 can be extended to model both the physics of PET and SPECT detection and the statistical fluctuations due to noise.

Rather than simply assume a strip integral model as in (36), we can instead use the matrix relating image and data to more exactly model the probability,  $P_{ij}$ , of detecting an emission from voxel site  $j$  at detector element  $i$  [26, 29]. To differentiate this probabilistic model from the strip integral one, we will denote the detection probability matrix

by  $\mathbf{P}$ . The elements of this matrix are dependent on the specific data acquisition geometry and other factors such as detector efficiency, attenuation effects within the subject, and the underlying physics of gamma ray emission for SPECT or positron-electron annihilation for PET.

In PET and SPECT the mean of the data can be estimated for a particular image as the linear transformation

$$E(\mathbf{y}) = \mathbf{P}\mathbf{f} \quad (38)$$

where  $\mathbf{f}$  represents the mean emission rates from each image voxel. In practice, these data are corrupted by additive noise terms due to scatter and either “random coincidences” in PET [7] or background radiation in SPECT [6]. The methods described below can be modified relatively easily to include these factors but these issues will not be addressed further here. See [27] and [28] for a more in depth review of these and other factors that affect statistical reconstruction methods in PET and SPECT.

In both PET and SPECT, external radiation sources are used to perform transmission measurements. These are used to correct for attenuation in the emission studies. Just as in x-ray CT, it is possible to reconstruct an image of attenuation coefficients from these transmission measurements. In this case, the unknown image  $\mathbf{f}$  is the set of attenuation coefficients for each voxel and the transition probability matrix  $\mathbf{P}$ , in the simplest case, has elements  $P_{ij}$  equal to the fractional intersection of the  $i$ th projection ray with the  $j$ th voxel. If  $E(\mathbf{y})$  represents the mean value of the transmission measurement, and assuming that the source intensity is a constant  $\alpha$ , then we can model the mean of the transmission data as:

$$E(y_i) = \alpha \exp \left\{ - \sum_j P_{ij} f_j \right\} \quad (39)$$

For both emission and transmission measurements, the data can be modeled as collections of independent Poisson random variables, mean  $E(\mathbf{y})$ , with joint probability:

$$p(\mathbf{y}/\mathbf{f}) = \prod_{i=1}^M \frac{E(y_i)^{y_i} e^{-E(y_i)}}{y_i!} \quad (40)$$

The physical model for the detection system is included in the likelihood function in the mapping from the image  $\mathbf{f}$  to the mean of the detected events  $E(\mathbf{y})$  using (38) and (39) for the transmission and emission case respectively. Using this basic model, we can develop estimators based on maximum likelihood or Bayesian image estimation principles.

## 6.3 Maximum Likelihood Methods

The maximum likelihood estimator is the image that maximizes the likelihood (40) over the set of feasible images,  $\mathbf{f} \geq \mathbf{0}$ .

The EM (expectation maximization) algorithm can be applied to the emission CT problem resulting in an iterative algorithm which has the elegant closed form update equation [30]:

$$f_j^{n+1} = \frac{f_j^n}{\sum_i P_{ij}} \sum_i \frac{P_{ij} y_i}{\sum_l P_{il} f_l^n} \quad (41)$$

This algorithm has a number of interesting properties including the fact that the solution is naturally constrained by the iteration to be non-negative. Unfortunately, the method tends to exhibit very slow convergence and is often unstable at higher iterations. The variance problem is inherent in the ill-conditioned Fisher information matrix. This effect can be reduced using *ad hoc* stopping rules where the iterations are terminated before convergence. An alternative approach to reducing variance is through penalized maximum likelihood or Bayesian methods as described in Section 6.4.

A number of modifications of the EM algorithm have been proposed to speed up convergence. The most widely used of these is the ordered subsets EM (OSEM) algorithm in which each iteration uses only a subset of the data [31]. Let  $\{S_k\}$ ,  $k = 1, \dots, Q$ , be a disjoint partition of the set  $\{1, 2, \dots, M\}$  representing the indices of the data. Let  $n$  denote the iteration number, defined as the number of complete cycles through the  $Q$  subsets, and define  $f_j^{(n,0)} = f_j^{(n-1,Q)}$ . Then one complete iteration of OSEM is given by:

$$f_j^{(n,k)} = \frac{f_j^{(n,k-1)}}{\sum_{i \in S_k} P_{ij}} \sum_{i \in S_k} \frac{P_{ij} y_i}{\sum_l P_{il} f_l^{(n,k-1)}} \quad \text{for } j = 1, \dots, N; \quad k = 1, \dots, Q \quad (42)$$

In the early iterations OSEM produces remarkable improvements in convergence rates compared to EM, although subsequent iterations over the entire data is required for ultimate convergence. The OSEM algorithm has now been widely adopted for reconstruction of clinical PET scans since it achieves significant improvements in image quality for photon limited data when compared to analytic methods, and does so in clinically acceptable reconstruction times. In the case of 3D PET, computation cost is further reduced by using the Fourier rebinning method of Section 4.3 to reduce the data to a set of 2D sinograms (one per axial slice) and then applying OSEM to each 2D slice in turn [32].

The corresponding ML problem for transmission data does not have a closed form EM algorithm. However, both emission and transmission ML problems can be solved effectively using standard gradient ascent approaches such as the conjugate gradient method. In fact, it is easily shown that the emission EM algorithm can also be written as a steepest descent algorithm with a diagonal preconditioner equal to the current image estimate [33].

In recent years, a great deal of progress has been made in developing fast algorithms for emission and transmission tomography that borrow ideas from both the EM and OSEM approaches to generate convergent algorithms. The EM algorithm can be viewed as one of a general class of "optimization transfer" methods [34]. These methods replace the original objective function  $\Phi(f; y)$  at each iteration with a surrogate function  $\Psi(f, f^n; y)$  that satisfies the following properties:

$$\Phi(f^n; y) = \Psi(f^n, f^n; y) \quad (43)$$

$$\Phi(f; y) \geq \Psi(f, f^n; y) \quad (44)$$

These two conditions in combination can be used to ensure that if  $f^{n+1}$  is chosen as the maximizer of  $\Psi(f, f^n; y)$ , then  $\Phi(f^n; y)$  is a non-decreasing sequence in  $f^n$ . The surrogates are chosen so that they are more easily optimized than the original objective at each iteration. Careful choice of these objective functions can lead to closed form update equations, even for the transmission reconstruction problem, and to faster convergence than that exhibited by the original EM algorithm.

The second approach to development of more rapidly converging algorithms is to use subsets of the data at each iteration. As implemented in the original OSEM algorithm this does not lead to convergence. However, it is possible to use this concept within a globally convergent framework. Methods of this type are referred to as "incremental gradient" methods and are based on rewriting the objective function as a sum over sub-objective functions [35]:

$$\Phi(f; y) = \sum_{k=1}^Q \Phi_k(f; y_k) \quad (45)$$

where  $\Phi_k(f; y_k)$  represents the portion of the objective function that is dependent only on the subset of the data:  $\{y_i : (i \in S_k)\}$ . Iteratively updating the image estimate with respect to each subobjective in turn and using an appropriate relaxation scheme can lead to rapid initial convergence and guarantee global convergence. Since the surrogate and incremental gradient approaches are general, they are applicable to both emission and transmission reconstruction, and also to both the maximum likelihood problem described above and the Bayesian or penalized maximum likelihood formulations described below.

## 6.4 Bayesian Reconstruction Methods

As noted above, direct maximum likelihood estimates of PET images exhibit high variance due to ill-conditioning. Some form of regularization is required to produce acceptable images. Often regularization is accomplished simply by starting with a smooth initial estimate and terminating a maximum likelihood search before convergence. Here we



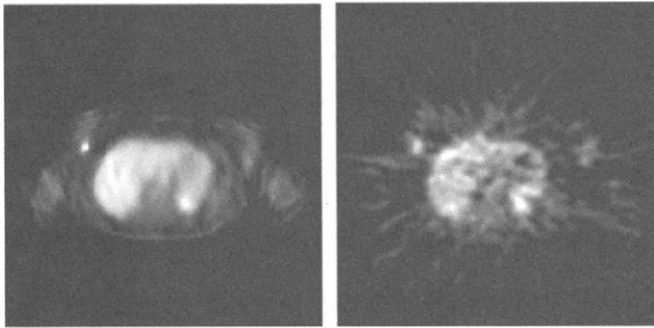


**FIGURE 14** Example of a PET scan of metabolic activity using FDG, an F-18 tagged analog of glucose. This tracer is used in detection of malignant tumors. The left image shows a reconstruction of a slice through the chest of a patient with breast cancer; the tumor is visible in the bright region in the upper left region of the chest. This image was reconstructed using the Bayesian method described in [29] and illustrates the improvement in image quality that can be realized using a statistically based approach, in comparison to a direct reconstruction method which was used to reconstruct the right image from the same data.

consider explicit regularization procedures in which a prior distribution is introduced through a Bayesian reformulation of the problem (see also Chapter 3.11). Some authors prefer to present these regularization procedures as penalized maximum likelihood methods but the differences are largely semantic.

By introduction of random field models for the unknown image, Bayesian methods can address the ill-posedness inherent in PET image estimation. In an attempt to capture the locally structured properties of images, researchers in emission tomography, and many other image processing applications, have adopted Gibbs distributions as a suitable class of prior [36]. The Markovian properties of these distributions make them both theoretically attractive as a formalism for describing empirical local image properties, as well as computationally appealing, since the local nature of their associated energy functions results in computationally efficient update strategies (see Chapter 4.2 for a description of Gibbs random field models for image processing). The majority of work using Gibbs distributions in tomographic applications involves relatively simple pair-wise interaction models where the Gibbs energy function is formed as a sum of potentials, each defined on neighboring pairs of pixels. These potential functions can be chosen to reflect the piecewise smooth property of many images. The existence of sharp intensity changes, corresponding to the edges of objects in the image, can also be modeled using more complex MRF models. The Bayesian formulation also offers the potential for combining data from multiple modalities. For example, high resolution anatomic x-ray CT or MR images can be used to improve the quality of reconstructions from low resolution PET or SPECT data [37].

Let  $p(f)$  denote the Gibbs prior that captures the expected statistical characteristics of the image. The posterior

probability for the image conditioned on the data is then given by Bayes theorem:

$$p(f|y) = \frac{p(y|f)p(f)}{p(y)} \quad (46)$$

Bayesian estimators in tomography are usually of the maximum *a posteriori* (MAP) type. The MAP solution is given by maximizing the posterior probability  $p(f|y)$  with respect to  $f$ . For each data set, the denominator of the right hand side of (46) is a constant so that the MAP solution can be found by maximizing the log of the numerator, i.e.,

$$\max_f \text{Ln } p(y|f) + \text{Ln } p(f) \quad (47)$$

A large number of algorithms have been developed for computing the MAP solution. The EM algorithm (41) can be extended to include a prior term (see for example [37]) and hence maximize (47). This algorithm suffers from the same slow convergence problems as (41). Alternatively, (47) can be maximized using standard nonlinear optimization algorithms such as the preconditioned conjugate gradient method [29] or coordinate-wise optimization [38]. The specific algorithmic form is found by applying these standard methods to (47) after substituting both the log of the likelihood function (40) in place of  $\text{Ln } p(y|f)$  and the log of the Gibbs density in place of  $\text{Ln } p(f)$ . Alternatively, optimization transfer and incremental gradient methods can be modified to include prior distribution and have been used effectively to design rapidly converging algorithms. For compound Gibbs priors that involve line-processes, mean field annealing techniques can be combined with any of the above methods [28, 37]. Figure 14 shows an example of PET image reconstruction where the combination of the Poisson likelihood function and a Gibbs prior produce significant improvements in image quality over a reconstruction using the filtered backprojection algorithm.

## 7 Summary

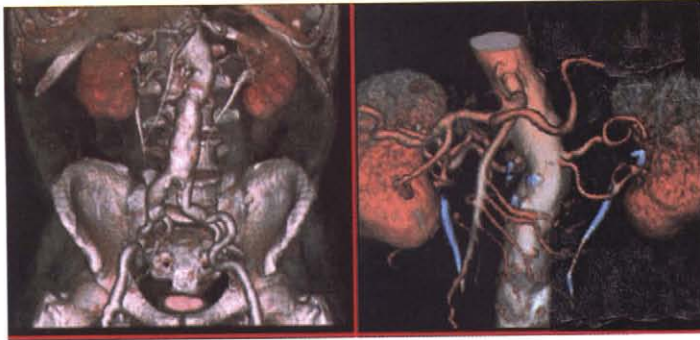
We have summarized direct and iterative approaches to 2D and 3D tomographic reconstruction for x-ray CT, PET and SPECT. With the exception of the rebinning algorithms, which can be used in place of fully 3D reconstruction methods, the choice of direct reconstruction algorithm is determined primarily by the data collection geometry. On the other hand, the iterative approaches (ART, ML and MAP) can be applied to any collection geometry in PET and SPECT. Furthermore, after appropriate modifications to account for differences in the mapping from image to data, these methods are also applicable to transmission PET and SPECT data. X-ray CT data are not Poisson so that a different likelihood model is required if ML or MAP methods are to be used.

Image processing for computed tomography remains an active area of research. In large part development is driven by construction of new imaging systems which are continuing to improve the resolution of these technologies. Carefully tailored reconstruction algorithms will help to realize the full potential of these new systems. In the realm of x-ray CT, new spiral and cone-beam systems are extending the capabilities of CT systems to allow fast volumetric imaging for medical and other applications. In PET and SPECT, recent developments are also aimed at achieving high resolution volumetric imaging through combinations of new detector and collimator designs with fast, accurate reconstruction algorithms. In addition to advances resulting from new instrumentation developments, current areas of intense research activity include theoretical analysis of algorithm performance, combining accurate modeling with fast implementations of iterative methods, direct methods that account for factors not included in the line integral model, and development of methods for fast dynamic volumetric (4D) imaging.

## References

- [1] H. H. Barrett and W. Swindell, *Radiological Imaging, Vols. I and II*, New York: Academic Press, 1981.
- [2] S. Webb, *From the Watching of Shadows: The Origins of Radiological Tomography*, Institute of Physics, Institute of physics publishing, 1990.
- [3] H. P. Hiriyanaiyah, X-ray computed tomography, *IEEE Signal Processing Magazine*, 14(2):42–59, 1997.
- [4] A. C. Kak and M. Slaney, *Principles of Computerized Tomographic Imaging*, New York: IEEE Press, 1988.
- [5] S. Webb (ed.), *The Physics of Medical Imaging*, London: Institute of Physics, 1988.
- [6] G. Gullberg, G. Zeng, F. Datz, R. Christian, C. Tung, and H. Morgan, Review of convergent beam tomography in single photon emission computed tomography, *Phys. Med. Biol.*, 37:507–534, 1992.
- [7] S. R. Cherry and M. E. Phelps, Imaging brain function with positron emission tomography, in *Brain Mapping: the Methods*, A. W. Toga and J. C. Mazziotta (eds.), New York: Academic Press, 1996.
- [8] D. MacLaren, T. Toyokuni, S. Cherry, J. Barrio, M. E. Phelps, H. R. Herschman, and S. S. Gambhir, PET imaging of transgene expression, *Biological Psychiatry*, 48(5):337–348, 2000.
- [9] S. R. Cherry, Y. Shao, R. W. Silverman, K. Meadors, S. Siegel, A. Chatzioannou, et al., MicroPET: A high resolution PET scanner for imaging small animals, *IEEE Trans. Nucl. Sci.*, 44:1161–1166, 1997.
- [10] B. Bendriem and D. W. Townsend (eds), *The Theory and practice of 3D PET*, Kluwer, 1998.
- [11] L. A. Shepp and B. F. Logan, The Fourier reconstruction of a head section, *IEEE Trans. Nucl. Sci.*, NS-21:21–33, 1974.
- [12] B. K. Horn, Fan-beam reconstruction methods, *Proc. IEEE*, 67: 1616–1623, 1979.
- [13] G. Besson, CT fan-beam parameterizations leading to shift-invariant filtering, *Inverse Problems*, 12:815–833, 1996.
- [14] F. Noo, M. Defrise, R. Clackdoyle, and H. Kudo, Image reconstruction from fan-beam projections on less than a short scan, *Phys. Med. Biol.*, 47:2525–2546, 2002.
- [15] R. Clackdoyle and F. Noo, A large class of inversion formulae for the Radon transform of functions of compact support, *Inverse Problems*, 20:1281–1291, 2004.
- [16] C. Crawford and K. King, Computed tomography scanning with simultaneous patient translation, *Medical Physics*, 17:967–982, 1990.
- [17] M. Daube-Witherspoon and G. Muehllehner, An iterative image space reconstruction algorithm suitable for volume ECT, *IEEE Trans. Med. Imag.*, 5:61–66, 1986.
- [18] M. Defrise, P. Kinahan, D. Townsend, C. Michel, M. Sibomana, and D. Newport, Exact and approximate rebinning algorithms for 3D PET data, *IEEE Trans. Med. Imag.*, 16:145–158, 1997.
- [19] J. Colsher, Fully three dimensional positron emission tomography, *Phys. Med. Biol.*, 25:103–115, 1980.
- [20] P. Kinahan and L. Rogers, Analytic 3D image reconstruction using all detected events, *IEEE Trans. Nucl. Sci.*, NS-36:964–968, 1996.
- [21] L. Feldkamp, L. Davis, and J. Kress, Practical cone-beam algorithm, *J. Optical Soc. Amer., A*, 1:612–619, 1984.
- [22] P. Grangeat, Mathematical framework for cone-beam three-dimensional image reconstruction via the first derivative of the Radon transform, *Mathematical Methods in Tomography (Lecture Notes in Mathematics, vol. 1497)*, ed. G. Herman, A. Louis, and F. Natterer, (Berlin: Springer) 66:97, 1991.
- [23] M. Defrise and R. Clack, A cone-beam reconstruction algorithm using shift-variant filtering and cone-beam backprojection, *IEEE Trans. Med. Imag.*, 13:186–95, 1994.
- [24] G. T. Herman, *Image Reconstruction From Projections: The Fundamentals of Computerized Tomography*, New York: Academic Press, 1980.
- [25] Y. Censor, Finite series-expansion reconstruction methods, *Proc. IEEE*, 71: 409–419, 1983.
- [26] M. Smith, C. Floyd, R. Jaszczak, and E. Coleman, Three-dimensional photon detection kernels and their application to SPECT reconstruction, *Phys. Med. Biol.*, 37:605–622, 1992.
- [27] J. M. Ollinger and J. A. Fessler, Positron emission tomography, *IEEE Sig. Proc. Mag.*, 14(1):43–55, 1997.
- [28] R. Leahy and J. Qi, Statistical approaches in quantitative PET, to appear, *Statistics and Computing*, 10:147–165, 2000.
- [29] J. Qi, R. Leahy, S. Cherry, A. Chatzioannou, and T. Farquhar, High resolution 3D bayesian image reconstruction using the microPET small animal scanner, *Phys. Med. Biol.*, 43(4):1001–1013, 1998.
- [30] A. Shepp and Y. Vardi, Maximum likelihood reconstruction for emission tomography, *IEEE Trans. Med. Imag.*, 2:113–122, 1982.
- [31] H. Hudson and R. Larkin, Accelerated image reconstruction using ordered subsets of projection, *IEEE Trans. Med. Imag.*, 13:601–609, 1994.
- [32] C. Comtat, P. E. Kinahan, M. Defrise, C. Michel, and D. W. Townsend, Fast reconstruction of 3D PET data with accurate statistical modeling, *IEEE Transactions on Nuclear Science*, 45:1083–1089, 1998.

- [33] L. Kaufman, Maximum likelihood, least squares, and penalized least squares for PET, *IEEE Trans. Med. Imag.*, 12:200–214, 1993.
- [34] K. Lange, D. R. Hunter, and I. Yang, Optimization transfer using surrogate objective functions (with discussion), *J. Comput. Graphical Stat.*, 9:1–59, 2000.
- [35] S. Ahn and J. A. Fessler, Globally convergent image reconstruction for emission tomography using relaxed ordered subsets algorithms, *IEEE Trans. Med. Imag.*, 22(5):613–626, 2003.
- [36] S. Geman and D. McClure, Statistical methods for tomographic image reconstruction, *Proceedings of the 46th Session of the International Statistical Institute, Bulletin of the ISI*, 52:4–20, 1987.
- [37] G. Gindi, M. Lee, A. Rangarajan, and I. G. Zubal, Bayesian reconstruction of functional images using anatomical information as priors, *IEEE Trans. Med. Imag.*, 12:670–680, 1993.
- [38] J. Fessler, Hybrid polynomial objective functions for tomographic image reconstruction from transmission scans, *IEEE Trans. Image. Proc.*, 4:1439–1450, 1995.



**FIGURE 10.2.5** Volume rendering from a sequence of x-ray CT images showing the abdominal cavity and kidneys (CT images courtesy of G. E. Medical Systems).

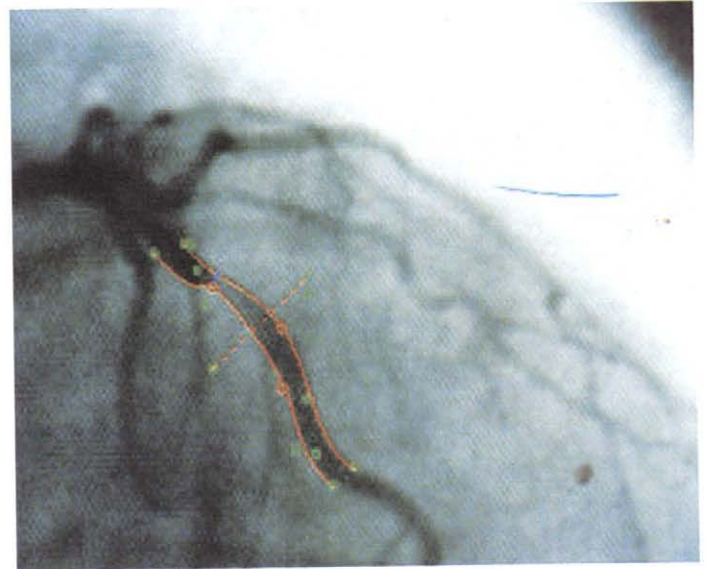


**FIGURE 10.3.3** Result of active-contour analysis applied to a selected artery in a typical 2-D angiogram. The green points are the manually identified control points. The red lines are the computed vessel wall borders. From [9].

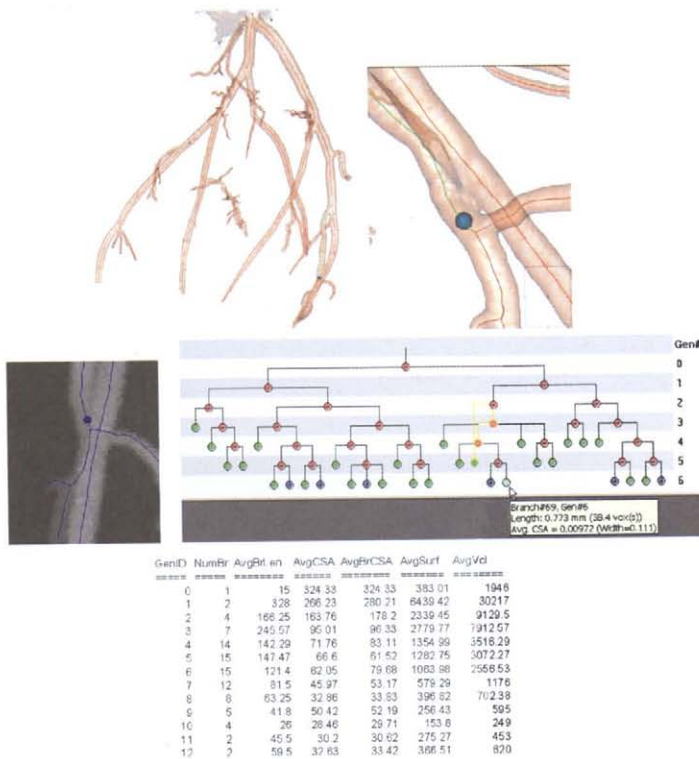


**FIGURE 10.3.6** Composite view of system for analyzing a 3-D arterial tree [19]. (a) Surface-rendered version of the extracted 3-D arterial tree; a tree defect is marked by a ball; in all views the lines denote the tree central axes. (b) Local surface rendering of tree about the selected defect. (c) Local depth-weighted slab of original 3-D gray-scale data about defect. (d) Quantitative description of final tree [18]. (e) Graph of corrected tree; nodes signify branch points; circles with plusses signifying graph nodes that can be expanded further; a node (branch) is selected to show its local quantitative description.

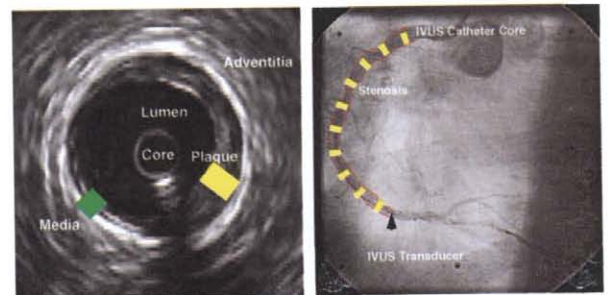


**FIGURE 10.3.8** Angiographic and IVUS views of the coronary arteries. Right view is a 2-D angiogram; arrow indicates location of the IVUS transducer. Left view shows corresponding cross-sectional IVUS frame of the arterial lumen. (Figure courtesy of Dr. Andreas Wahle, University of Iowa.)